The Electronic Realization of Synchronous Machines: Model Matching, Angle Tracking, and Energy Shaping Techniques

Catalin Arghir and Florian Dörfler

***Abstract*—In this article, we investigate grid-forming and grid-following control strategies starting from a nonlinear state-space modeling viewpoint. An electronic synchronous machine is an inverter whose integral of the dc-bus measurement generates the angle of the instantaneous modulation vector. We show how this minimal augmentation constitutes an exact physical realization without requiring inner-current loops. The dc-link capacitance becomes the equivalent rotational inertia of the converter. Additional features, such as a phase locked loop, a voltage controller, and a power tracking mechanism are then designed via two energy-shaping techniques. One energy function is used to implement a grid-following control scheme, via the inherent synchronizing torque, while the other is used to implement a grid-forming control scheme. An alternative interpretation of active-power droop is suggested by this method. The results are first derived systematically, and then evaluated experimentally on a front-to-front setup.**

***Index Terms*—Angle synchronization, converter control, electronic synchronous machine (eSM), grid forming, grid following.**

I. Introduction

THE fundamental frequency is widely regarded as an indicator for power imbalance in machine-dominated grids. We develop a framework showing how the dc-bus measurement can complement that basis in future power grids.

In three-phase systems, energy typically flows through several conversion stages, such as a magnetic air gaps or switching devices, circulates in passive circuits, and is bound to satisfy certain requirements. Most energy conversion aspects [1], such as the modulation of power from one to two dimensions (i.e., from dc to ac) and the stabilization of the required harmonic motion, are addressed by VSCs operating in grid-forming or grid-following mode [2]. The typical VSC controllers employ inner loops, which perform high-gain regulation of the quantities of interest from the input source to the point of power injection [3]. The power balance is achieved via multiple time scales running in the feedback path, which settle at the appropriate steady state. However, the large number of states of the inner loops makes the analysis of multiple converters difficult [4], motivating the study of more direct control approaches, [5], [6].

With the growing complexity of the power system at large [7], [8], the cascaded control structure can give rise to poorly understood interactions, causing phase locked loop (PLL) instabilities and oscillations of various kinds [9]. Toward the goal of improving overall system stability, virtual synchronous machines (VSMs) of various degrees of fidelity [10]–[12], are deployed to emulate inertia and damping features. The VSM controller assigns set points to the existing inner loops so that the currents and voltages behave according to a numerical model, often disregarding the dc link of the converter. In an increasingly underdamped converter landscape, impedance-based techniques [13], [14] explore the effects of PLLs, while comparative studies [4], [15], [16] show postfault shortcomings of the conventional, small-signal approach.

In the mean time, control-theoretic advances brought more and more physical elements in the feedback design [17], [18], allowing modeling, control, and stability analysis to be performed systematically. These methods, focused on stabilization of (networked) electromechanical systems, can provide insightful solutions for many complex problems arising in power conversion, and allow robust regulation without requiring inner loops, while providing guarantees on the quantities of interest. In this aim, we combine two control approaches: that of passivity-based control [17], exploiting the fundamental energy balance property, and that of output regulation [19], invoking the internal model principle.

In this article, we start from the paradigm first reported in [20] and [21], and propose a nonlinear, large-signal treatment of the factors leading to physical, as opposed to numerical, synchronous machine (SM) emulation. We show to what extent the machine dynamics are matched, via a coordinate transformation between the SM and the VSC state-space models. In an independent and parallel study [22], [23], we highlight the analogy between the electromotive force (EMF) and air-gap torque of the SM, and the equivalent quantities of the inverter. Furthermore, we consider the reactive component of the air-gap torque, constituting the inherent SM synchronization mechanism, and construct an alternative for the PLL. We also show how active-power droop naturally emerges as a synchronizing torque by minimizing an energy function. We aim to provide a unifying

Manuscript received March 12, 2019; revised June 21, 2019; accepted August 20, 2019. Date of publication September 4, 2019; date of current version January 10, 2020. This work was supported in part by the ETH Zürich funds and in part by the SNF under the Assistant Professor Energy under Grant 160573. Recommended for publication by Associate Editor R. Burgos. *(Corresponding author: Catalin Arghir.)*

The authors are with the Automatic Control Laboratory, ETH Zürich, 8092 Zürich, Switzerland (e-mail: carghir@control.ee.ethz.ch; dorfler@ethz.ch).

Color versions of one or more of the figures in this article are available online at http://ieeexplore.ieee.org.

Digital Object Identifier 10.1109/TPEL.2019.2939710

framework for control and stability analysis of grid-forming and grid-following behavior.

In contrast to similar studies [24]–[26], this article illustrates several ways in which large-signal synchronization can occur. An outcome of our design is a direct angle control scheme, similar in complexity to direct power control (DPC) [27], [28], which omits inner-current loops and offers fast control of active and reactive power. In our case, the power set point is achieved by appropriately controlling the converter angle, while still allowing a current controller to work in parallel rather than in cascade. This distinctive feature is the result of replacing reference tracking by a less restrictive nonlinear control design, related to geometric path following [18]. Finally, this article provides a control design method, a stability certification, and an experimental validation.

The rest of this article is organized as follows. Notation is introduced then, in Section II, the structural equivalence is presented. Section III offers a solution to the single machine infinite bus problem used in grid following, while Section IV presents a grid-forming design. Before concluding, Section V provides experimental results from a small-scale microgrid.

A. Preliminaries and Notation

We consider a three-phase, two-level active bridge driven by pulsewidth modulation (PWM) with complementary duty-cycle ratios, given as $d_{\mathrm{a}}(t)$, $d_{\mathrm{b}}(t)$, and $d_{\mathrm{c}}(t)$, each taking values from 0 to 1 during a switching cycle. By denoting the column vector $\boldsymbol{d}_{\mathrm{abc}} = [d_{\mathrm{a}}, d_{\mathrm{b}}, d_{\mathrm{c}}]$, we only focus on the continuous-time average-switch behavior and disregard the switching-frequency harmonics. Furthermore, by adopting space vector modulation (SVM) terminology, we define the instantaneous modulation vector as

$$\boldsymbol{m}_{\mathrm{abc}}(t) = \boldsymbol{d}_{\mathrm{abc}}(t) - \left[\frac{1}{2}, \frac{1}{2}, \frac{1}{2}\right]. \tag{1}$$

We write this modulation vector in *machine orientation*, via its polar representation relative to the stationary frame as

$$\boldsymbol{m}_{\mathrm{abc}}(t) = m(t) \begin{bmatrix} -\sin\left(\theta(t)\right) \\ -\sin\left(\theta(t) - \frac{2\pi}{3}\right) \\ -\sin\left(\theta(t) + \frac{2\pi}{3}\right) \end{bmatrix} \tag{2}$$

where $m(t) \in [0, \frac{1}{2}]$ and $\theta(t) \in [-\pi, \pi)$ are the instantaneous SVM magnitude and angle. We consider the *power-invariant* $\alpha\beta$ transformation and omit the zero sequence. Accordingly, $\boldsymbol{m}_{\alpha\beta}(t) = \sqrt{\frac{2}{3}} \begin{bmatrix} 1 & -\frac{1}{2} & -\frac{1}{2} \\ 0 & \frac{\sqrt{3}}{2} & -\frac{\sqrt{3}}{2} \end{bmatrix} \boldsymbol{m}_{\mathrm{abc}}(t)$ is defined so that

$$\boldsymbol{m}_{\alpha\beta}(t) = \mu(t) \begin{bmatrix} -\sin\theta(t) \\ \cos\theta(t) \end{bmatrix} \tag{3}$$

where $\mu(t) = \sqrt{3/2} m(t)$ denotes the modulation magnitude in this $\alpha\beta$ frame. Furthermore, we write the identity matrix as $\mathbf{I} = \left[\begin{smallmatrix} 1 & 0 \\ 0 & 1 \end{smallmatrix}\right]$ and the rotation matrix as $\mathbf{R}_{\phi} = \left[\begin{smallmatrix} \cos\phi & -\sin\phi \\ \sin\phi & \cos\phi \end{smallmatrix}\right]$. Given a two-dimensional vector $\boldsymbol{x} = \left[\begin{smallmatrix} x_1 \\ x_2 \end{smallmatrix}\right]$, we define its magnitude as $\|\boldsymbol{x}\| = \sqrt{x_1^2 + x_2^2}$. We shall also make use of the partial differential operator $\frac{\partial}{\partial x} = \nabla$ when x is a scalar (will always be an angle variable), and $\frac{\partial}{\partial \boldsymbol{x}} = [\frac{\partial}{\partial x_1} \ \frac{\partial}{\partial x_2}]$ as a row vector, when $\boldsymbol{x}$ is a two-dimensional column vector.

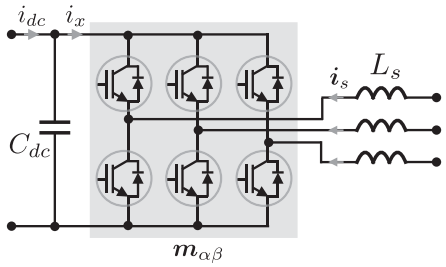

Fig. 1. Inverter depicted with its dc-link capacitor and switched inductor.

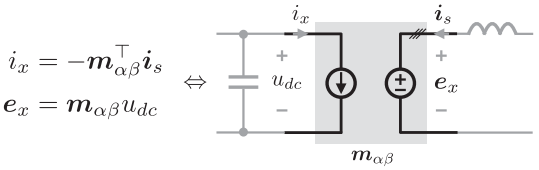

Fig. 2. Core element of an inverter: The dc–ac energy transformation mechanism, satisfying power balance $u_{\mathrm{dc}} i_x + \boldsymbol{e}_x^{\top} \boldsymbol{i}_s = 0$, and modulated by the two-dimensional signal $\boldsymbol{m}_{\alpha\beta}$.

II. Inverter-Machine Equivalence

To study the fundamental energy modulation mechanism of inverters and electrical machines alike, we adopt a stationary frame and identify the structural equivalence between the two.

A. VSC Model

Considering the dc-supply current i_{dc} and the ac-grid voltage $\boldsymbol{v}_g$ as external inputs, we model the VSC

$$C_{\mathrm{dc}} \frac{\mathrm{d}u_{\mathrm{dc}}}{\mathrm{d}t} = -G_{\mathrm{dc}} u_{\mathrm{dc}} + i_{\mathrm{dc}} + \boldsymbol{m}_{\alpha\beta}^{\top} \boldsymbol{i}_s \tag{4a}$$

$$L_s \frac{\mathrm{d}\boldsymbol{i}_s}{\mathrm{d}t} = -R_s \boldsymbol{i}_s + \boldsymbol{v}_g - \boldsymbol{m}_{\alpha\beta} u_{\mathrm{dc}} \tag{4b}$$

in $\alpha\beta$ frame, where, apart from the elements in Fig. 1, G_{dc} is a parallel conductance modeling (switching) losses in the dc link, while R_s models the (conduction) losses in series with the switching inductor.

We consider the main nonlinearity to be the power-preserving structure shown in Fig. 2, where the average switch current drawn from the dc link is denoted by i_x, while the ac-side average-switch voltage is denoted by $\boldsymbol{e}_x$. These quantities will be related to the SM air-gap torque and, respectively, the EMF.

Note that the signal $\boldsymbol{m}_{\alpha\beta}$, regardless of the control law, cannot inject or extract energy into the system. It acts in a lossless manner. To see this, we define the storage function

$$\mathcal{H} = \frac{1}{2} C_{\mathrm{dc}} u_{\mathrm{dc}}^2 + \frac{1}{2} \boldsymbol{i}_s^{\top} L_s \boldsymbol{i}_s \tag{5}$$

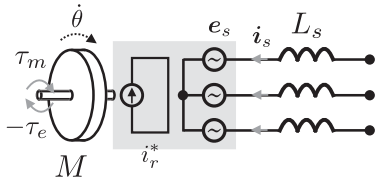

Fig. 3. SM with constant excitation, satisfying the lossless energy transfer property $\omega\tau_e + \boldsymbol{e}_s^\top \boldsymbol{i}_s = 0$, and modulated by the one-dimensional signal i_r^*.

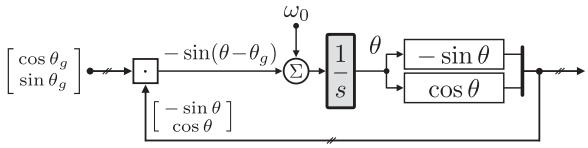

Fig. 4. Prototypical structure of a (unit gain) PLL showing the synchronization torque $-\sin(\theta-\theta_g)$. Here $\cdot$ denotes the vector dot product.

and observe that the change in total energy occurring during any evolution of system (4) does not depend on $\boldsymbol{m}_{\alpha\beta}$

$$\begin{aligned}\frac{\mathsf{d}\mathcal{H}}{\mathsf{d}t} &= C_{\rm dc}u_{\rm dc}\frac{\mathsf{d}u_{\rm dc}}{\mathsf{d}t} + \boldsymbol{i}_s^\top L_s\frac{\mathsf{d}\boldsymbol{i}_s}{\mathsf{d}t}\\ &= \underbrace{-G_{\rm dc}u_{\rm dc}^2 - \boldsymbol{i}_s^\top R_s\boldsymbol{i}_s}_{\text{internal dissipation}} + \underbrace{i_{\rm dc}u_{\rm dc} + \boldsymbol{i}_s^\top\boldsymbol{v}_g}_{\text{external injection}}\,. \end{aligned} \tag{6}$$

As we shall see, the role of $\boldsymbol{m}_{\alpha\beta}$ is to streamline the flow from the dc side into the grid– an energy transfer property.

B. SM Model

Consider the model of an SM having constant rotor excitation, whose derivation is presented in Appendix A

$$\frac{\mathsf{d}\theta}{\mathsf{d}t} = \omega \tag{7a}$$

$$M\frac{\mathsf{d}\omega}{\mathsf{d}t} = -D\omega + \tau_m + L_m i_r^*\begin{bmatrix}-\sin\theta\\ \cos\theta\end{bmatrix}^\top \boldsymbol{i}_s \tag{7b}$$

$$L_s\frac{\mathsf{d}\boldsymbol{i}_s}{\mathsf{d}t} = -R_s\boldsymbol{i}_s + \boldsymbol{v}_g - L_m i_r^*\begin{bmatrix}-\sin\theta\\ \cos\theta\end{bmatrix}\omega\,. \tag{7c}$$

The energy transfer now occurs in the machine air gap, modulated by the excitation current i_r^*, as shown in Fig. 3

$$\tau_e = -L_m i_r^*\begin{bmatrix}-\sin\theta\\ \cos\theta\end{bmatrix}^\top \boldsymbol{i}_s \tag{8a}$$

$$\boldsymbol{e}_s = L_m i_r^*\begin{bmatrix}-\sin\theta\\ \cos\theta\end{bmatrix}\omega\,. \tag{8b}$$

In a conventional PLL design [29], as well as in some simplified SM models [4], the electrical torque (8a) is represented by $\sin(\theta-\theta_g)$, where θ_g is the angle of the grid voltage. See also Fig. 4. This is what we later call the synchronizing torque since, upon closer inspection, it appears as an energy minimization term, motivating the study in the remainder of this article.

The matching control law presented next is designed to synthesize all elements of the SM model (7) using corresponding elements of the inverter model (4), upon augmenting an integrator in the closed loop. As illustrated in (6), due to its energy-conservation property, $\boldsymbol{m}_{\alpha\beta}$ cannot be used to implement a lossy element, such as a damper winding. This is why we restrict ourselves to matching the ideal SM with constant excitation current.

C. Electronic SM (eSM)

We start by denoting ω_0 as the nominal angular velocity, corresponding to the grid frequency, and $u_{\rm dc}^*$ as the reference dc-link voltage, related to the grid voltage level. Consider system (4), for which we use the modulation (3) to identify a similar energy-conversion structure as in the SM

$$i_x = -\mu\begin{bmatrix}-\sin\theta\\ \cos\theta\end{bmatrix}^\top \boldsymbol{i}_s \tag{9a}$$

$$\boldsymbol{e}_x = \mu\begin{bmatrix}-\sin\theta\\ \cos\theta\end{bmatrix}u_{\rm dc}\,. \tag{9b}$$

This key analogy prompts us to augment (4) with an integrator for the dc-link voltage in the same way that, in the mechanical domain, the rotor angle integrates the angular velocity (11a)

$$\frac{\mathsf{d}\theta}{\mathsf{d}t} = \eta u_{\rm dc}\,. \tag{10}$$

By choosing the scaling factor $\eta = \omega_0/u_{\rm dc}^*$, we define the equivalent angular velocity of the inverter as $\omega = \eta u_{\rm dc}$. Here, η converts units of voltage into units of angular velocity, but also units of torque into units of current. This coordinate transformation allows us to select the constant modulation magnitude $\mu = \eta L_m i_r^*$ in (3) and complete the exact model-matching design by identifying $i_x/\eta = \tau_e$ and $\boldsymbol{e}_x = \boldsymbol{e}_s$ with the SM air-gap torque and EMF (8), respectively.

We are now able to rewrite, via $\omega = \eta u_{\rm dc}$, the closed-loop system (3), (4), (10) referred to as the eSM

$$\frac{\mathsf{d}\theta}{\mathsf{d}t} = \omega \tag{11a}$$

$$\frac{C_{\rm dc}}{\eta^2}\frac{\mathsf{d}\omega}{\mathsf{d}t} = -\frac{G_{\rm dc}}{\eta^2}\omega + \frac{i_{\rm dc}}{\eta} + \frac{\mu}{\eta}\begin{bmatrix}-\sin\theta\\ \cos\theta\end{bmatrix}^\top \boldsymbol{i}_s \tag{11b}$$

$$L_s\frac{\mathsf{d}\boldsymbol{i}_s}{\mathsf{d}t} = -R_s\boldsymbol{i}_s + \boldsymbol{v}_g - \frac{\mu}{\eta}\begin{bmatrix}-\sin\theta\\ \cos\theta\end{bmatrix}\omega\,. \tag{11c}$$

By comparing (11) to (7), we further identify the equivalent mechanical torque $i_{\rm dc}/\eta = \tau_m$, rotor moment of inertia $C_{\rm dc}/\eta^2 = M$ and rotor damping coefficient $G_{\rm dc}/\eta^2 = D$. Consequently, the inertia introduced by this model-matching control corresponds to instantaneous physical energy stored in the dc link. Moreover, the magnetization factor appears as $\mu/\eta = L_m i_r^*$, while the stator self-inductance L_s of the SM is identified with the switching-side inductance of the inverter.

As a general guideline, to achieve a nominal EMF voltage amplitude $\|\boldsymbol{e}_s\| = e_0$, the rotor excitation can be chosen as $i_r^* =$

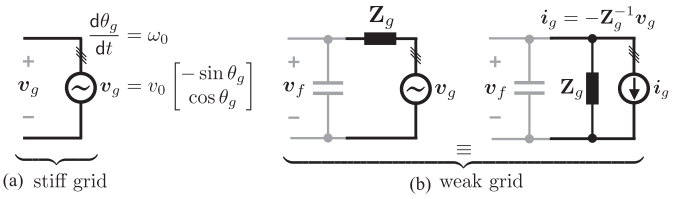

Fig. 5. Two types of ac buses considered. (a) Stiff voltage source. (b) Local ac capacitor charged by a distant source and its Norton equivalent. Throughout this article, $\boldsymbol{v}_g$ and $\boldsymbol{i}_g$ will be sinusoidal of constant amplitude and constant frequency ω_0.

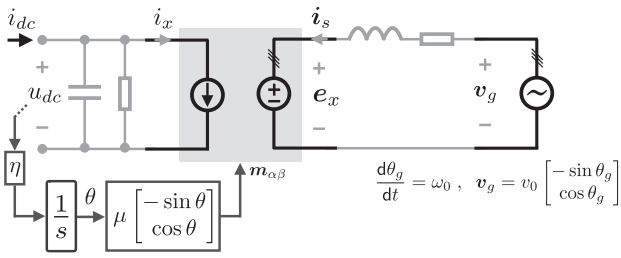

Fig. 6. Equivalent circuit of the eSM (11) connected to a stiff grid.

$e_0/(\omega_0 L_m)$, from which we can determine $\mu = e_0/u_{\mathrm{dc}}^*$. As we shall see in the rest of this article, the value of μ can be adjusted to achieve additional objectives for the eSM.

D. Inertia and Damping Augmentation

Compared to rotating machinery, the power-electronics-sourced dc-current i_{dc} has a much faster actuation bandwidth than the valve of a turbine governor. This dc input can implement, for instance, a standard proportional integral derivative (PID) control of the form

$$i_{\mathrm{dc}} = -K_p(u_{\mathrm{dc}} - u_{\mathrm{dc}}^*) - K_i x_{\mathrm{dc}} - K_d \frac{\mathrm{d}u_{\mathrm{dc}}}{\mathrm{d}t} \tag{12a}$$

$$\frac{\mathrm{d}x_{\mathrm{dc}}}{\mathrm{d}t} = u_{\mathrm{dc}} - u_{\mathrm{dc}}^* \tag{12b}$$

where x_{dc} is the state of the integrator. The gains K_p and K_d add extra damping and inertia to the terms G_{dc} and C_{dc}, respectively, in (11), contributing physically to the energy balance. In the following sections, we will replace the conventional integral term with an explicit precomputation of the steady-state bias.

E. Frequency Behavior of the eSM

The eSM enables the coupling between ac frequency and dc voltage, allowing the inverter to function without a conventional PLL and in both stiff and weak grids, such as in Fig. 5. Broadly speaking, in a stiff grid, the internal eSM frequency adapts to an external frequency by charging or discharging its dc-link voltage. Alternatively, if the grid does not impose a certain frequency, the dc-link maintains its nominal value, and the eSM forms the system frequency. Thus, adopting the grid-following or grid-forming classifications, the eSM can function in either mode.

In the following sections, we make these ideas precise and study the large-signal behavior. We first treat the stiff and weak grid cases separately, discussing two ways in which synchronization naturally emerges. Finally, we combine the two in an experiment, where the frequency is not driven by an external source.

III. Synchronization to a Stiff Grid

Our goal now is to determine the current injection i_{dc} which, in conjunction with the matching modulation $\boldsymbol{m}_{\alpha\beta}$, achieves three basic control objectives: (i) dc-bus regulation; (ii) angle synchronization; (iii) internal stability. Although there are situations in which the dc current is not available as a control input, but rather acts as a disturbance, our framework is general enough to provide an informative solution.

Consider the inverter connected to a stiff ac-bus voltage given by a sinusoidal signal of constant amplitude v_0 and constant frequency ω_0, as in Fig. 6. The power flow is directly reflected in the relationship between the internal voltage vector $\boldsymbol{e}_x$ and the grid voltage $\boldsymbol{v}_g$, seen at the terminals of the eSM. To control the angle difference between these two vectors, we construct an energy function, whose minimization is performed by the inherent eSM synchronizing torque.

A. eSM Synchronizing Torque

Observe that, when the dc bus is firmly regulated, namely, when $u_{\mathrm{dc}} = u_{\mathrm{dc}}^*$, the switching-node voltage $\boldsymbol{e}_x$ becomes sinusoidal, of constant amplitude μu_{dc}^*, and frequency ηu_{dc}^*, which, for a steady-state solution to exist, must be equal to ω_0. In this case, the inductor current (4b) attains a sinusoidal solution as $t \to \infty$. Thus, we say that the stiff angle dynamics (both θ and θ_g) are dominant[1] and induce a *steady-state response*. In accordance with the internal model principle [30], we express this as the angle-dependent solution

$$\hat{\boldsymbol{i}}_s = \mathbf{Z}_s^{-1}\left(\boldsymbol{v}_g - \mu u_{\mathrm{dc}}^* \begin{bmatrix} -\sin\theta \\ \cos\theta \end{bmatrix}\right) \tag{13}$$

where $\mathbf{Z}_s = \left[\begin{smallmatrix} R_s & -\omega_0 L_s \\ \omega_0 L_s & R_s \end{smallmatrix}\right]$, its inverse is $\mathbf{Z}_s^{-1} = \|\mathbf{Z}_s\|^{-2}\mathbf{Z}_s^\top$ and its matrix norm $\|\mathbf{Z}_s\| = \sqrt{R_s^2 + \omega_0^2 L_s^2}$. In general, when the dc bus is in transient, (13) only represents a steady-state preview signal and serves as an analysis tool.

In order to maintain the dc bus at steady state, the upstream injection i_{dc} must adopt a suitable internal model, i.e. a feedforward bias, which we can derive from the switching current

$$\begin{aligned} \hat{i}_x &= -\boldsymbol{m}_{\alpha\beta}^\top \hat{\boldsymbol{i}}_s \\ &= -\mu \begin{bmatrix} -\sin\theta \\ \cos\theta \end{bmatrix}^\top \mathbf{Z}_s^{-1}\left(\boldsymbol{v}_g - \mu u_{\mathrm{dc}}^* \begin{bmatrix} -\sin\theta \\ \cos\theta \end{bmatrix}\right) \end{aligned}$$

[1] i.e., lacking any form of dissipation, having the slowest decay rate.

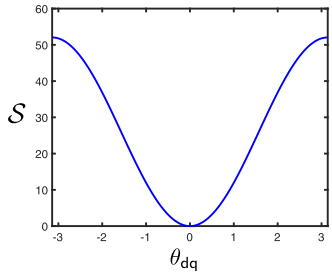

Fig. 7. Plot of the synchronization potential $\mathcal{S}$ as a function of $\theta_{\mathsf{dq}} = \theta - \theta_g$, with minimum at 0 and maximum at $\pm\pi$.

$$= \underbrace{\frac{\mu v_0 R_s}{\|\mathbf{Z}_s\|^2}\left(\frac{\mu u_{\mathrm{dc}}^*}{v_0} - \cos(\theta-\theta_g)\right)}_{(a)} + \underbrace{\frac{\mu v_0 \omega_0 L_s}{\|\mathbf{Z}_s\|^2}\sin(\theta-\theta_g)}_{(b)}. \tag{14}$$

The relevance of this formulation is that it provides a guideline for angle synchronization. By commanding i_{dc} to account solely for term (a), corresponding to the active part of $\hat{i}_x$, the closed loop would only feature the reactive part (b). We call this the inherent synchronizing torque of the eSM.

Observe that the term (b) can be also expressed as the gradient of a quadratic function. We call this the *synchronization potential*, as it anticipates the energy stored in the inductor. The proposed energy function takes the form

$$\begin{aligned}\mathcal{S} &= \frac{1}{2}\hat{\boldsymbol{i}}_s^\top L_s \hat{\boldsymbol{i}}_s \\ &= \frac{1}{2}\frac{L_s}{\|\mathbf{Z}_s\|^2}\left(\mu^2 u_{\mathrm{dc}}^{*2} - 2\mu u_{\mathrm{dc}}^* v_0 \cos(\theta-\theta_g) + v_0^2\right).\end{aligned} \tag{15}$$

In essence, we aim to drive the angle difference $\theta_{\mathsf{dq}} = \theta - \theta_g$ to a value, which minimizes the energy function $\mathcal{S}$, as seen in Fig. 7. While in this case the minimizer represents zero angle difference, we will later provide a way to achieve a more general operating point.

The internal model variables $\hat{\boldsymbol{i}}_s$ and $\hat{i}_x$, can be computed in real time from the angle variables. They are also useful in constructing transient dynamics and stability certificates.

B. Error-Coordinates Analysis

We now pursue a systematic design procedure for the dc-side control law i_{dc} by formulating a stabilization problem for the error dynamics of the eSM system. Consider the grid-attached dq frame $\theta_{\mathsf{dq}} = \theta - \theta_g$ and $\boldsymbol{i}_{\mathsf{dq}} = \mathbf{R}_{\theta_g}^\top \boldsymbol{i}_s$. In these coordinates, the internal model (13) becomes a function of the angle difference θ_{dq}. By defining $\hat{\boldsymbol{i}}_{\mathsf{dq}}(\theta_{\mathsf{dq}}) = \mathbf{R}_{\theta_g}^\top \hat{\boldsymbol{i}}_s$ and

$$\mathcal{S}(\theta_{\mathsf{dq}}) = \frac{1}{2}\hat{\boldsymbol{i}}_{\mathsf{dq}}(\theta_{\mathsf{dq}})^\top L_s \hat{\boldsymbol{i}}_{\mathsf{dq}}(\theta_{\mathsf{dq}}) \tag{16}$$

we are able to express the control specifications in terms of driving the error system to zero as $t \to \infty$.

1) DC-bus regulation: $u_{\mathrm{dc}} \to u_{\mathrm{dc}}^*$.
2) Angle synchronization:[2] $\theta_{\mathsf{dq}} \to \theta_{\mathsf{dq}}^*$ s.t. $\nabla\mathcal{S}(\theta_{\mathsf{dq}}^*) = 0$.

[2]Throughout this article, ∇ will always be taken w.r.t. the variable θ_{dq}.

3) Internal stability: $\boldsymbol{i}_{\mathsf{dq}} \to \hat{\boldsymbol{i}}_{\mathsf{dq}}(\theta_{\mathsf{dq}})$.

In essence, the energy-based control technique presented in Appendix B considers the dynamics of the error coordinates, as well as a shifted energy function derived from (5). This ultimately leads to the stabilizing control law

$$i_{\mathrm{dc}} = \underbrace{-K_p(u_{\mathrm{dc}} - u_{\mathrm{dc}}^*)}_{\text{P-control}} + \underbrace{G_{\mathrm{dc}} u_{\mathrm{dc}}^* + \hat{i}_x(\theta_{\mathsf{dq}})}_{\text{steady-state bias}} \underbrace{-\eta\nabla\mathcal{S}(\theta_{\mathsf{dq}})}_{\text{synchronization}} \tag{17}$$

by adding damping, matching the appropriate terms, and, respectively, minimizing the potential energy. The task of producing this current is carried out by the upstream converter, typically a boost or an active rectifier. The proposed controller achieves objective (iii) indirectly: By stabilizing the dc voltage, the appropriate steady state is consequently induced.

From a physical point of view, the steady-state bias, together with the synchronization term, represent a feedforward injection of the ac-side losses anticipated by the internal model

$$\hat{i}_x(\theta_{\mathsf{dq}}) - \eta\nabla\mathcal{S}(\theta_{\mathsf{dq}}) = \hat{\boldsymbol{i}}_s^\top R_s \hat{\boldsymbol{i}}_s \tag{18}$$

and can be computed in stationary frame via (13). It actually performs the cancelation of the term (a). What remains in the closed loop is the error term $i_x - \hat{i}_x$, and the synchronizing torque

$$\eta\nabla\mathcal{S}(\theta_{\mathsf{dq}}) = \frac{\mu v_0 \omega_0 L_s}{\|\mathbf{Z}_s\|^2}\sin\theta_{\mathsf{dq}} \tag{19}$$

corresponding to the term (b), the reactive part of $\hat{i}_x$.

To focus on the angle behavior, we neglect the inductor current transients, i.e., we assume that $\boldsymbol{i}_{\mathsf{dq}} = \hat{\boldsymbol{i}}_{\mathsf{dq}}(\theta_{\mathsf{dq}})$, hence also $i_x = \hat{i}_x(\theta_{\mathsf{dq}})$, for all time, and consider subsystem (11a) and (11b) with input (17)

$$\frac{\mathrm{d}\theta_{\mathsf{dq}}}{\mathrm{d}t} = \eta\tilde{u}_{\mathrm{dc}} \tag{20a}$$

$$C_{\mathrm{dc}}\frac{\mathrm{d}\tilde{u}_{\mathrm{dc}}}{\mathrm{d}t} = -(G_{\mathrm{dc}} + K_p)\tilde{u}_{\mathrm{dc}} - \eta\nabla\mathcal{S}(\theta_{\mathsf{dq}}) \tag{20b}$$

where $\tilde{u}_{\mathrm{dc}} = u_{\mathrm{dc}} - u_{\mathrm{dc}}^*$. In this way, the eSM can be seen as analogous to a damped pendulum where the tangential component of gravity (corresponding to the gradient term) drives the mass to a rest position having zero angle with respect to the downward vertical axis (corresponding to the grid voltage vector here). This mechanical analogy, shown in Fig. 8, is also known as the *swing equations*, an important tool in studying synchronization in power networks [31].

This is also represented as block diagram in Fig. 9. Alternatively, the proposed PLL can be seen as a second-order gradient descent, an algorithm which settles when the gradient vanishes. Among the configurations where $\nabla\mathcal{S}(\theta_{\mathsf{dq}}) = 0$, the point of interest is the stable equilibrium $\theta_{\mathsf{dq}} = 0$.

To account for inductor current transients, an energy-based stability analysis is pursued in Appendix B, by considering the error $\tilde{\boldsymbol{i}}_{\mathsf{dq}} = \boldsymbol{i}_{\mathsf{dq}} - \hat{\boldsymbol{i}}_{\mathsf{dq}}(\theta_{\mathsf{dq}})$, and the energy function

$$\tilde{\mathcal{H}}(\theta_{\mathsf{dq}}, \tilde{u}_{\mathrm{dc}}, \tilde{\boldsymbol{i}}_{\mathrm{dc}}) = \frac{1}{2}C_{\mathrm{dc}}\tilde{u}_{\mathrm{dc}}^2 + \mathcal{S}(\theta_{\mathsf{dq}}) + \frac{1}{2}\tilde{\boldsymbol{i}}_{\mathsf{dq}}^\top L_s \tilde{\boldsymbol{i}}_{\mathsf{dq}}. \tag{21}$$

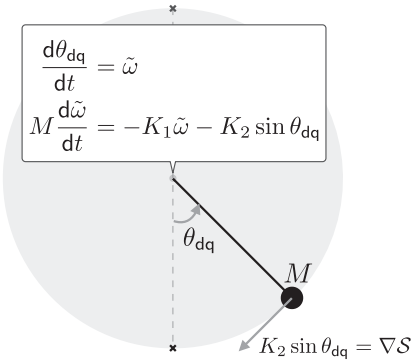

Fig. 8. eSM system (11) in feedback with (17), when $\boldsymbol{i}_{\mathsf{dq}} = \hat{\boldsymbol{i}}_{\mathsf{dq}}$, shown in error coordinates $\tilde{\omega} = \eta\tilde{u}_{\mathrm{dc}}$. Here, $M = C_{\mathrm{dc}}/\eta^2$ and $K_1 = (C_{\mathrm{dc}} + K_p)/\eta^2$ are related to the pendulum moment of inertia and damping.

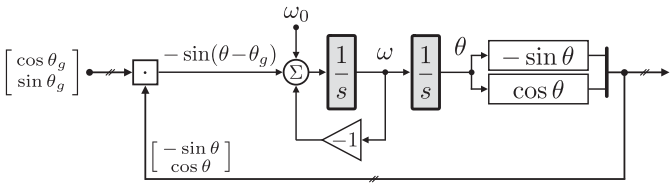

Fig. 9. Prototypical structure of a second-order PLL showing the synchronization torque $-\sin(\theta-\theta_g)$, and the additional state variable ω, where $\omega \to \omega_0$ along with $\theta \to \theta_g$, as $t \to \infty$. Both the PLL gain and the time constant of ω are set to 1 for simplicity of exposition.

This extends the nonlinear stability proof of the damped pendulum to the eSM with inductor dynamics, thus guaranteeing the control objectives. The analysis suggests that, in order to prevent full revolutions of the angle, sufficient (active) damping must be present on the dc link.

Remark 1: (Mode-switching feature) From Fig. 9, we see that the primary distinction to conventional PLL design is that the state $\omega = \eta u_{\mathrm{dc}}$ is represented by the dc voltage of the inverter. By looking at (19), we also notice that the gain of the synchronizing torque depends on the grid voltage magnitude, $\|\boldsymbol{v}_g\| = v_0$. When the grid is absent, this term vanishes and so the converter angle is driven solely by the dc bus, which tracks the reference $u^*_{\mathrm{dc}} = \omega_0/\eta$. In this way, the converter switches from grid-following to grid-forming mode.

C. Direct Angle Control

There are scenarios in which the upstream converter cannot provide any further degree of freedom other than dc-bus regulation. We can design an alternative, first-order angle synchronization mechanism, by replacing the controller defined by the pair (10) and (17) with

$$\frac{\mathrm{d}\theta}{\mathrm{d}t} = \eta u_{\mathrm{dc}} - \kappa'\nabla\mathcal{S} \tag{22a}$$

$$i_{\mathrm{dc}} = -K_p(u_{\mathrm{dc}} - u^*_{\mathrm{dc}}) + G_{\mathrm{dc}}u^*_{\mathrm{dc}} + \hat{i}_x \tag{22b}$$

where κ' plays the role of a PLL gain. When compared to (20), the transients are similar and settle at the same equilibrium. The main advantage is that, effectively, the gain κ' is implemented purely in software and is decoupled from the damping injection K_p, subject to the control bandwidth limitations of the upstream converter. In this case, the entire expression (22b) can be replaced by a conventional PID design. Finally, exact matching no longer occurs as the gradient term resembles the slip torque of an induction machine.

D. PQ Set-Point Tracking

The proposed control structure (17) so far achieves zero angle difference between $\boldsymbol{e}_x$ and $\boldsymbol{v}_g$. This is due to the construction of the function $\mathcal{S}$, having its minimum at $\theta^*_{\mathsf{dq}} = 0$. Building on top of that, we can design μ and modify the potential energy $\mathcal{S}$ to allow an arbitrary operating point. Let us define the instantaneous active and reactive powers, and their internal-model counterparts (also depending on θ_{dq}), as

$$\begin{aligned} P_g &= -\boldsymbol{i}_s^\top \boldsymbol{v}_g & \hat{P}_g(\theta_{\mathsf{dq}}) &= -\hat{\boldsymbol{i}}_s^\top \boldsymbol{v}_g \\ Q_g &= -\boldsymbol{i}_s^\top \begin{bmatrix} 0 & 1 \\ -1 & 0 \end{bmatrix} \boldsymbol{v}_g & \hat{Q}_g(\theta_{\mathsf{dq}}) &= -\hat{\boldsymbol{i}}_s^\top \begin{bmatrix} 0 & 1 \\ -1 & 0 \end{bmatrix} \boldsymbol{v}_g \,. \end{aligned} \tag{23}$$

Assuming we are given a set point (P^*_g, Q^*_g), we aim to find the corresponding μ^* and θ^*_{dq}, which further achieves power tracking as $t \to \infty$. The overall control objectives become the following.

1) DC-bus regulation: $u_{\mathrm{dc}} \to u^*_{\mathrm{dc}}$.
2) PQ tracking: $\theta_{\mathsf{dq}} \to \theta^*_{\mathsf{dq}}$ s.t. $(\hat{P}_g, \hat{Q}_g)(\theta^*_{\mathsf{dq}}) = (P^*_g, Q^*_g)$.
3) Internal stability: $\boldsymbol{i}_{\mathsf{dq}} \to \hat{\boldsymbol{i}}_{\mathsf{dq}}(\theta_{\mathsf{dq}})$.

Notice that, when all three objectives are satisfied, the modulation settles at a constant magnitude μ^* and an angle θ^* rotating with constant angular velocity ω_0, just like the grid angle. Since we can define $\theta^*_{\mathsf{dq}} = \theta^* - \theta_g$, the inductor current producing the desired power injection $P^*_g = \hat{P}_g(\theta^*_{\mathsf{dq}})$, $Q^*_g = \hat{Q}_g(\theta^*_{\mathsf{dq}})$ corresponds to $\boldsymbol{i}^*_{\mathsf{dq}} = \hat{\boldsymbol{i}}_{\mathsf{dq}}(\theta^*_{\mathsf{dq}})$. We are able to compute this quantity in $\alpha\beta$ frame as $\boldsymbol{i}^\star_s = \mathbf{R}_{\theta_g}\boldsymbol{i}^*_{\mathsf{dq}}$, via the grid measurement $\boldsymbol{v}_g = (v_{g_\alpha}, v_{g_\beta})$

$$\boldsymbol{i}^\star_s = \frac{1}{\|\boldsymbol{v}_g\|^2}\begin{bmatrix} v_{g_\alpha} & v_{g_\beta} \\ -v_{g_\beta} & v_{g_\alpha} \end{bmatrix}\begin{bmatrix} P^*_g \\ Q^*_g \end{bmatrix} \tag{24}$$

from which we extract the features of the modulation vector

$$\mu^* = \frac{1}{u^*_{\mathrm{dc}}}\|\boldsymbol{v}_g - \mathbf{Z}_s\boldsymbol{i}^\star_s\| \tag{25a}$$

$$\begin{bmatrix} -\sin\theta^* \\ \cos\theta^* \end{bmatrix} = \frac{1}{\mu^* u^*_{\mathrm{dc}}}\left(\boldsymbol{v}_g - \mathbf{Z}_s\boldsymbol{i}^\star_s\right). \tag{25b}$$

This calculation can also be seen in the block diagram of Fig. 10. Finally, we use $\mu = \mu^*$ in $\boldsymbol{m}_{\alpha\beta}$, and by replacing $\mathcal{S}(\theta_{\mathsf{dq}})$ with $\mathcal{S}(\theta_{\mathsf{dq}} - \theta^*_{\mathsf{dq}})$, we modify controller (17) as follows:

$$i_{\mathrm{dc}} = -K_p\tilde{u}_{\mathrm{dc}} + G_{\mathrm{dc}}u^*_{\mathrm{dc}} + \hat{i}_x(\theta_{\mathsf{dq}}) - \eta\nabla\mathcal{S}(\theta_{\mathsf{dq}} - \theta^*_{\mathsf{dq}}). \tag{26}$$

The synchronization torque can be computed in $\alpha\beta$ frame

$$\begin{aligned} \nabla\mathcal{S}(\theta_{\mathsf{dq}} - \theta^*_{\mathsf{dq}}) &= \frac{\mu^* v_0\omega_0 L_s}{\eta\|\mathbf{Z}_s\|^2}\begin{bmatrix} -\sin\theta \\ \cos\theta \end{bmatrix}^\top \begin{bmatrix} 0 & 1 \\ -1 & 0 \end{bmatrix}\begin{bmatrix} -\sin\theta^* \\ \cos\theta^* \end{bmatrix} \\ &= \frac{\mu^* v_0\omega_0 L_s}{\eta\|\mathbf{Z}_s\|^2}\sin(\theta - \theta^*). \end{aligned} \tag{27}$$

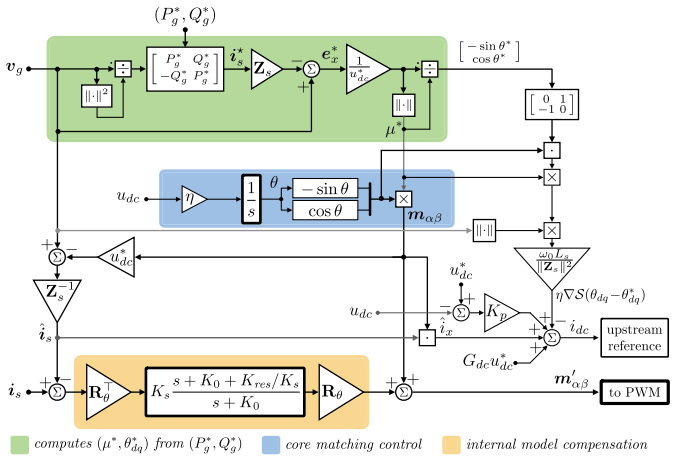

Fig. 10. Block diagram of the PQ set point tracking controller (10), (26), (28). Here, i_{dc} is given as a reference for the output current of the upstream converter and $\boldsymbol{m}'_{\alpha\beta}$ is the modulation signal sent to the PWM.

Since the dc-link voltage, the angle difference and the inductor current stabilize in the same manner as before, we have that all three objectives are attained simultaneously, without requiring the assumption of time-scale separation and without tracking $\boldsymbol{i}_s^\star$ directly. The nonlinear stability analysis in Appendix B pertains when replacing $\mathcal{S}(\theta_{\mathsf{dq}})$ with $\mathcal{S}(\theta_{\mathsf{dq}} - \theta^*_{\mathsf{dq}})$ in the Hamiltonian function (21).

E. Internal Model Correction

Due to model uncertainty in formulas, such as (13) and later (31), the internal model representation can become inaccurate, resulting in a misaligned steady-state operation. One way to correct this is to actively pursue objective (iii). In this aim, the modulation vector can be augmented with a proportional-resonant controller enforcing $\boldsymbol{i}_s \to \hat{\boldsymbol{i}}_s$ as $t \to \infty$

$$\begin{aligned} \boldsymbol{m}'_{\alpha\beta} &= \mu^* \begin{bmatrix} -\sin\theta \\ \cos\theta \end{bmatrix} + K_s(\boldsymbol{i}_s - \hat{\boldsymbol{i}}_s) + K_{res}\mathbf{R}_\theta \boldsymbol{x}_{dq} \\ \frac{\mathsf{d}\boldsymbol{x}_{dq}}{\mathsf{d}t} &= -K_0 \boldsymbol{x}_{\mathsf{dq}} + \mathbf{R}_\theta^\top (\boldsymbol{i}_s - \hat{\boldsymbol{i}}_s). \end{aligned} \tag{28}$$

Here K_s is the gain of the proportional term, and K_{res} is the gain of an integral term implemented in the dq-frame rotating with the eSM angle θ, while K_0 is used to limit the dc gain of the integrator. Controller (28), seen in yellow in Figs. 10 and 11, is responsible for compensating the feedforward strategy. In a parallel loop, matching-control produces the path variable $\hat{\boldsymbol{i}}_s$ and its associated feedforward injection. For a simpler implementation, $\boldsymbol{i}_s^\star$ may be used instead of $\hat{\boldsymbol{i}}_s$.

Alternatively, by employing the first-order control structure (22) for the PQ-tracking case (see Fig. 11), we obtain a direct angle control method, similar in complexity to carrier-based DPC. Due to the flexibility of direct angle control (22), the gain $\kappa = \kappa' \frac{\mu^* v_0 \omega_0 L_s}{\eta \|\mathbf{Z}_s\|^2}$ in Fig. 11 can be tuned via κ'.

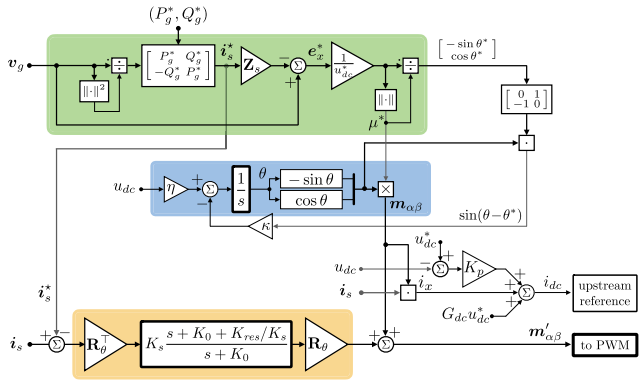

Fig. 11. Block diagram of the modified PQ set point tracking controller (22), (28), where $\hat{\boldsymbol{i}}_s$ is replaced by $\boldsymbol{i}_s^\star$ and $\hat{i}_x$ by i_x to show a simpler alternative.

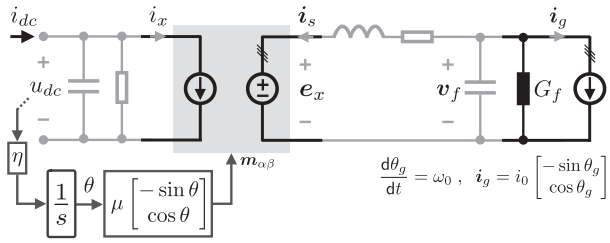

Fig. 12. Equivalent circuit of the eSM connected to a weak grid.

F. Extension to Multiple Circuit Elements

Consider the case of an inverter with an LCL filter, i.e. consisting of a switching-side inductor L_{s_1}, a shunt capacitor C_f, and a grid-side inductor L_{s_2}. The extension of this methodology is done by including the dynamics of the filter elements and their associated internal model solutions $\hat{\boldsymbol{i}}_{s_1}$, $\hat{\boldsymbol{v}}_f$, and $\hat{\boldsymbol{i}}_{s_2}$. The synchronization potential (16) then becomes

$$\mathcal{S}(\theta_{\mathsf{dq}}) = \frac{1}{2}\hat{\boldsymbol{i}}_{s_1}^\top L_{s_1} \hat{\boldsymbol{i}}_{s_1} - \frac{1}{2}\hat{\boldsymbol{v}}_f^\top C_f \hat{\boldsymbol{v}}_f + \frac{1}{2}\hat{\boldsymbol{i}}_{s_2}^\top L_{s_2} \hat{\boldsymbol{i}}_{s_2}\,. \tag{29}$$

This typically yields a similar gradient as in Fig. 7, but with the minimum shifted slightly away from zero. We refer to [32] for the multi-inverter extension to networks with inductive edges and capacitive nodes.

IV. Regulation of a Weak Grid

We now turn to the second scenario. The inverter is required to regulate the ac voltage of a (local) weak bus to a given amplitude v_f^*. To include in our analysis the ac-bus dynamics, we augment (4) with a three-phase capacitor to ground, to which we attach a parallel admittance (resistive for simplicity) and a sinusoidal current source modeling the presence of another converter, or a weak grid, as shown in Fig. 12; see also the equivalent circuit in Fig. 5. We have

$$\frac{\mathsf{d}\theta}{\mathsf{d}t} = \eta u_{\mathrm{dc}} \tag{30a}$$

$$C_{\mathrm{dc}} \frac{\mathsf{d}u_{\mathrm{dc}}}{\mathsf{d}t} = -G_{\mathrm{dc}} u_{\mathrm{dc}} + i_{\mathrm{dc}} + \mu \begin{bmatrix} -\sin\theta \\ \cos\theta \end{bmatrix}^\top \boldsymbol{i}_s \tag{30b}$$

$$L_s \frac{\mathrm{d}\boldsymbol{i}_s}{\mathrm{d}t} = -R_s \boldsymbol{i}_s + \boldsymbol{v}_f - \mu \begin{bmatrix} -\sin\theta \\ \cos\theta \end{bmatrix} u_{\mathrm{dc}} \tag{30c}$$

$$C_f \frac{\mathrm{d}\boldsymbol{v}_f}{\mathrm{d}t} = -G_f \boldsymbol{v}_f - \boldsymbol{i}_s - \boldsymbol{i}_g \tag{30d}$$

where C_f is the ac-filter capacitance, G_f represents the combined resistive losses and loads associated to the ac bus, while the load current $\boldsymbol{i}_g$ represents a measurable vector of constant magnitude i_0, rotating at constant velocity ω_0.

A. Voltage Control and Grid-Forming Behavior

Similarly to Section III-A, we start by considering a well-regulated dc bus and the sinusoidal current source $\boldsymbol{i}_g$ defined in Fig. 12. The steady-state response induced by the stiff angle dynamics is expressed in $\alpha\beta$ frame as

$$\hat{\boldsymbol{i}}_s = -(\mathbf{Y}_f^{-1} + \mathbf{Z}_s)^{-1}\big(\mu u_{\mathrm{dc}}^* \begin{bmatrix} -\sin\theta \\ \cos\theta \end{bmatrix} + \mathbf{Y}_f^{-1}\boldsymbol{i}_g\big) \tag{31a}$$

$$\hat{\boldsymbol{v}}_f = (\mathbf{Z}_s\mathbf{Y}_f + \mathbf{I})^{-1}\big(\mu u_{\mathrm{dc}}^* \begin{bmatrix} -\sin\theta \\ \cos\theta \end{bmatrix} - \mathbf{Z}_s\boldsymbol{i}_g\big) \tag{31b}$$

where $\mathbf{Y}_f = \left[\begin{smallmatrix} G_f & -\omega_0 C_f \\ \omega_0 C_f & G_f \end{smallmatrix}\right]$ includes the grid admittance.

In the aim of regulating the voltage magnitude $\|\boldsymbol{v}_f\|$ to the set point v_f^*, we solve for the modulation length μ in (31b)

$$\hat{\mu}_f = \frac{\left[\begin{smallmatrix} -\sin\theta \\ \cos\theta \end{smallmatrix}\right]^\top \mathbf{Z}_s\boldsymbol{i}_g}{u_{\mathrm{dc}}^*} + \sqrt{\Big(\frac{\left[\begin{smallmatrix} -\sin\theta \\ \cos\theta \end{smallmatrix}\right]^\top \mathbf{Z}_s\boldsymbol{i}_g}{u_{\mathrm{dc}}^*}\Big)^2 + \frac{\|\mathbf{Z}_s\mathbf{Y}_f + \mathbf{I}\|^2 v_f^{*2} - \|\mathbf{Z}_s\boldsymbol{i}_g\|^2}{u_{\mathrm{dc}}^{*2}}}$$

by taking the positive solution of the quadratic equation $\hat{\boldsymbol{v}}_f^\top\hat{\boldsymbol{v}}_f = v_f^{*2}$. This solution exists if $\|\mathbf{Z}_s\mathbf{Y}_f + \mathbf{I}\|^2 v_f^{*2} - \|\mathbf{Z}_s\boldsymbol{i}_g\|^2 > 0$ holds [23]. Compared to (25a), $\hat{\mu}_f$ also requires the eSM angle θ apart from the grid measurement $\boldsymbol{i}_g$. By choosing $\mu = \hat{\mu}_f$, we have that $\|\hat{\boldsymbol{v}}_f\| = v_f^*$ for all time and, due to the internal stability property, $\|\boldsymbol{v}_f\| \to v_f^*$ as $t \to \infty$.

In this manner, we have decoupled ac-voltage control from angle behavior, thus enabling the grid forming operation. The dc-regulation requirement still needs to be carried out by i_{dc}, as in (22b) or via a PID design. Since the angle difference is left unregulated, the load current is able to extract an unbounded amount of active power (limited only by the dc source). In Section IV-B, we shall see how to control this power delivery.

B. Energy Shaping and Droop Control

We define the active and reactive power taken by $\boldsymbol{i}_g$ as

$$\begin{aligned} P_f &= \boldsymbol{i}_g^\top \boldsymbol{v}_f & \hat{P}_f(\theta_{\mathsf{dq}}) &= \boldsymbol{i}_g^\top \hat{\boldsymbol{v}}_f \\ Q_f &= \boldsymbol{i}_g^\top \begin{bmatrix} 0 & 1 \\ -1 & 0 \end{bmatrix} \boldsymbol{v}_f & \hat{Q}_f(\theta_{\mathsf{dq}}) &= \boldsymbol{i}_g^\top \begin{bmatrix} 0 & 1 \\ -1 & 0 \end{bmatrix} \hat{\boldsymbol{v}}_f \,. \end{aligned} \tag{32}$$

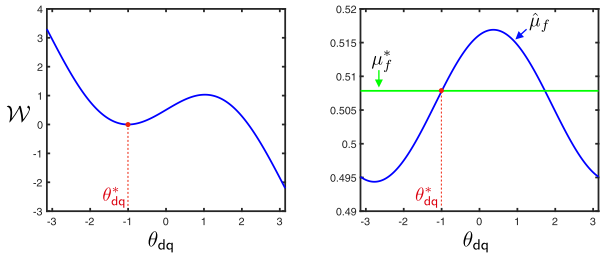

Fig. 13. Synchronization potential $\mathcal{W}$ (left) and the modulation lengths $\mu_f^* = \hat{\mu}_f(\theta^*_{\mathsf{dq}})$ and $\hat{\mu}_f$ (right) as functions of θ_{dq} for the set point $P_f^* = 326$ W, $v_f^* = 208$ V, corresponding to the minimizer $\theta^*_{\mathsf{dq}} = -1$.

Consider the scenario in which a power set point P_f^* is given in addition to v_f^*. The control objectives become the following.

1) DC-bus regulation: $u_{\mathrm{dc}} \to u_{\mathrm{dc}}^*$.
2) Grid support: $\theta_{\mathsf{dq}} \to \theta^*_{\mathsf{dq}}$ s.t. $\hat{P}_f(\theta^*_{\mathsf{dq}}) = P_f^*$, $\|\hat{\boldsymbol{v}}_f\| = v_f^*$.
3) Internal stability: $\boldsymbol{i}_s \to \hat{\boldsymbol{i}}_s$ and $\boldsymbol{v}_f \to \hat{\boldsymbol{v}}_f$.

By using the internal model relation (31b) in (32) and according to the steps shown in Appendix C, we obtain

$$\hat{P}_f(\theta_{\mathsf{dq}}) - \hat{P}_f(\theta^*_{\mathsf{dq}}) = \nabla\hat{Q}_f(\theta_{\mathsf{dq}}) - \nabla\hat{Q}_f(\theta^*_{\mathsf{dq}})\,. \tag{33}$$

This identity allows us to deduce a suitable synchronization energy function, via the Bregman divergence [33] of $\hat{Q}_f$

$$\mathcal{W}(\theta_{\mathsf{dq}}) = \frac{1}{\omega_0}\big(\hat{Q}_f(\theta_{\mathsf{dq}}) - \hat{Q}_f(\theta^*_{\mathsf{dq}}) - \nabla\hat{Q}_f(\theta^*_{\mathsf{dq}})(\theta_{\mathsf{dq}} - \theta^*_{\mathsf{dq}})\big)$$

seen in Fig. 13, which conveniently yields the gradient term

$$\nabla\mathcal{W}(\theta_{\mathsf{dq}}) = \frac{1}{\omega_0}\big(\nabla\hat{Q}_f(\theta_{\mathsf{dq}}) - \nabla\hat{Q}_f(\theta^*_{\mathsf{dq}})\big). \tag{34}$$

Remark 2: (Constant μ) In this subsection, we fix $\mu_f^* = \hat{\mu}_f(\theta^*_{\mathsf{dq}})$, given a set point (P_f^*, v_f^*). A constant modulation length, such as $\mu = \mu_f^*$ is technically required in the derivation of (33), but can be relaxed in practice. Alternatively, we can set $\mu = \frac{1}{u_{\mathrm{dc}}^*}\|\mathbf{Z}_s\mathbf{Y}_f + \mathbf{I}\|v_f^*$, in which case the amplitude $\|\boldsymbol{v}_f\|$ would droop with increasing load $\|\boldsymbol{i}_g\|$.

By using (33), we recover conventional, active-power droop as the synchronizing torque

$$\frac{1}{u_{dc}^*}(\hat{P}_f(\theta_{\mathsf{dq}}) - P_f^*) = \eta\nabla\mathcal{W}(\theta_{\mathsf{dq}}) \tag{35}$$

and reuse the control structure (17), with $\mathcal{W}$ instead of $\mathcal{S}$

$$i_{\mathrm{dc}} = \underbrace{-K_p(u_{\mathrm{dc}} - u_{\mathrm{dc}}^*)}_{\text{P-control}} + \underbrace{G_{\mathrm{dc}}u_{\mathrm{dc}}^* + \hat{i}_x}_{\text{steady-state bias}} \underbrace{-\eta\nabla\mathcal{W}(\theta_{\mathsf{dq}})}_{\text{synchronization}}\,. \tag{36}$$

The behavior is such that active-power droop drives θ_{dq} to the operating point where $\hat{P}_f(\theta^*_{\mathsf{dq}}) = P_f^*$. Finally, since (36) can be used in conjunction with $\mu = \mu_f^*$, we conclude that the set point (P_f^*, v_f^*) is achieved asymptotically as $t \to \infty$ via the energy minimization feature of gradient descent.

From an energy conservation perspective, if we define the steady-state ac losses as

$$\hat{P}_{\mathrm{loss}}(\theta_{\mathsf{dq}}) = \frac{1}{2}\hat{\boldsymbol{i}}_s^\top R_s\hat{\boldsymbol{i}}_s + \frac{1}{2}\hat{\boldsymbol{v}}_f^\top G_f\hat{\boldsymbol{v}}_f \tag{37}$$

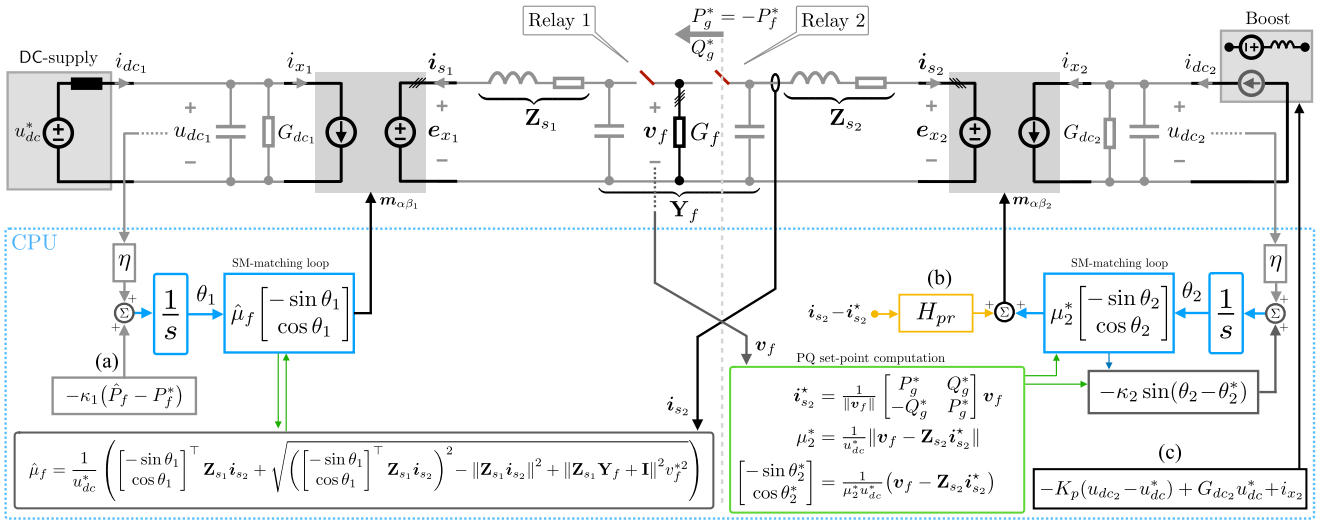

Fig. 14. Experiment implementation of the two-inverter system connected front to front. Index 1 denotes the grid forming and index 2 the grid-feeding unit. Here, (a) is optional and does not affect the normal operation, (b) is used, as described in Section III-E, to compensate for the model inaccuracy, and (c) is the control law implemented for i_{dc_2} via a boost converter.

we see that they are related to the dc-side current by

$$\hat{i}_x(\theta_{\mathsf{dq}}) = \frac{1}{u^*_{\mathrm{dc}}}\left(\hat{P}_{\mathrm{loss}}(\theta_{\mathsf{dq}}) + \hat{P}_f(\theta_{\mathsf{dq}})\right). \tag{38}$$

This, together with (35), allows us to reinterpret (36) as

$$i_{\mathrm{dc}} = \underbrace{-K_p\tilde{u}_{\mathrm{dc}}}_{\text{P-control}} + \frac{1}{u^*_{\mathrm{dc}}}\Big(\underbrace{G_{\mathrm{dc}}u^{*2}_{\mathrm{dc}} + \hat{P}_{\mathrm{loss}}(\theta_{\mathsf{dq}}) + P^*_f}_{\text{active power injection}}\Big) \tag{39}$$

which, as together with (18), suggests that, in order for large-signal synchronization to occur, the appropriate amount of active power must be injected from the dc side.

This formulation also reveals that in case of an overload, a saturation of i_{dc} would act as a curtailment in the effective set point P^*_f, corresponding to a reduction in angle difference, while still allowing the grid forming operation. This particular ability of matching control is also observed in [15] to survive large-load transients in situations where conventional cascaded-based and VSM controllers became unstable.

Remark 3: (Enabling droop control) As in Section III-C, the synchronizing torque can drive the eSM angle directly

$$\frac{\mathrm{d}\theta}{\mathrm{d}t} = \eta u_{\mathrm{dc}} - \underbrace{k\big(\hat{P}_f(\theta_{\mathsf{dq}}) - P^*_f\big)}_{k'\nabla\mathcal{W}} \tag{40}$$

where $k' = k\omega_0$ according to (35) and k is a PLL gain. This resembles standard droop control, the difference being that the ac-side frequency is replaced by the dc-bus measurement.

The stability analysis in Appendix B pertains when replacing $\mathcal{S}(\theta_{\mathsf{dq}})$ with $\mathcal{W}(\theta_{\mathsf{dq}})$ and extending the Hamiltonian analysis to account for the capacitor dynamics. Finally, both the stiff and weak grid scenarios are compatible with the two types of energy function, $\mathcal{S}$ or $\mathcal{W}$, upon appropriate choice of modulation μ, see Table I in the Appendix for a general overview.

V. Two-Converter Microgrid

So far we have seen two distinct behaviors, both offering the frequency support of an SM. In Section III-D, a grid-following mechanism tracks a PQ set point by assigning the modulation magnitude μ and its internal angle relative to a stiff bus. Then, in Section IV-B, a grid-forming mechanism regulates the ac-bus voltage via the modulation factor μ and, independently, the active power injection by regulating its internal angle relative to a sinusoidal disturbance. To validate experimentally the two systems, we set them up front to front, as seen in Fig. 14. Although both units feature an LC output filter, when shorted together, i.e., when the relays are closed, the two capacitors form a single ac bus to be regulated by the grid-forming unit (index 1), while the grid-feeding unit (index 2) injects active and reactive power and helps supply the load.

A. Experimental Setup

This experiment is performed on a general-purpose test-bench consisting of 8 IGBT half bridges [34], passive elements, 16 analog sensors, and a central processing unit (CPU) provided by Imperix SA. The parameters of the two inverters are as follows: $C_{\mathrm{dc}_{1,2}} = 1$ mF, $G_{\mathrm{dc}_{1,2}} = 9$ mS, $L_{s_{1,2}} = 1.5$ mH, $R_{s_{1,2}} = 1\,\Omega$, $C_{f_{1,2}} = 3.5\,\mu$F, and $G_f = 15.6$ mS. On the dc side, the two buses have independent, floating grounds, while on the ac side, the differential mode capacitors are connected in two different star points, independent from the star point of the resistive load.

The setup adopts the IEEE 60-Hz, 208-V line-to-line rms grid standard, at which the load conductance G_f draws 660 W, representing a light-load scenario. The CPU drives all PWM channels and samples all inductor currents and capacitor voltages at a frequency of 15.6 kHz, triggered at the peak of a symmetric triangular PWM carrier. The entire code, compiled from a Simulink.slx file, is executed in the same interrupt cycle for both units. All capture waveforms are signals from the CPU

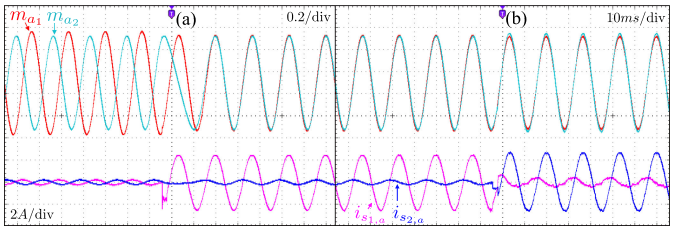

Fig. 15. Connecting G_f to the ac bus $\boldsymbol{v}_f$ of Unit 1 via Relay 1 (a), and then connecting Unit 2 via Relay 2 (b) while tracking set point $(P_g^*, Q_g^*) = (660, 0)$. Showing modulation, phase-a, of Unit 1 and of Unit 2, inductor current, phase-a, of Unit 1 and of Unit 2.

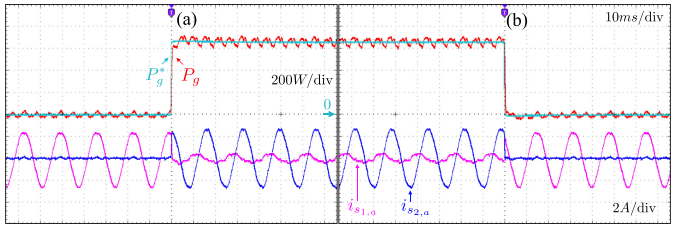

Fig. 16. Both relays remain closed while the set-point P_g^* for Unit 2 goes from 0 to 660 W at trigger (a) and then back to 0 at (b); $Q_g^* = 0$. Showing P_g^*, P_g, inductor current, phase-a, of Unit 1 and of Unit 2.

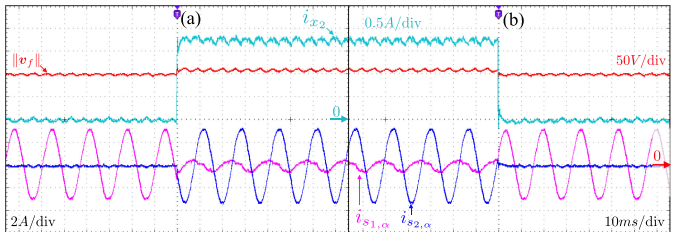

Fig. 17. Idem Fig. 16, P_g^* from 0 to 660 W (a) to 0 (b); $Q_g^* = 0$. Showing $\|\boldsymbol{v}_f\|$, i_{x_2}, inductor current, phase alpha, of Unit 1 and of Unit 2.

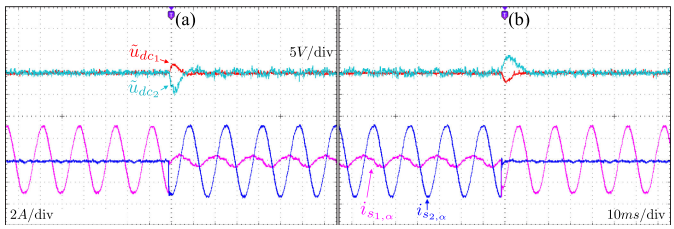

Fig. 18. Idem Fig. 16, P_g^* from 0 to 660W (a) to 0 (b); $Q_g^* = 0$. Showing $\tilde{u}_{\mathrm{dc}_1}$, $\tilde{u}_{\mathrm{dc}_2}$, inductor current, phase alpha, of Unit 1 and of Unit 2.

which are sent out, at every interrupt, via four digital-to-analog channels to the oscilloscope.

In Fig. 14, the source i_{dc_1} represents the current drawn from a dc lab power supply charging u_{dc_1} to 420 V. The current i_{dc_2} represents the reference given to an intermediate boost converter with the task of charging u_{dc_2} to $u_{\mathrm{dc}}^* = 420$ V via CPU-controlled PWM. The boost converter is supplied from a second dc-power supply and is placed upstream of inverter 2 in order to freely assign the dc-bus regulation strategy. The implementation is nonetheless according to Section III-C, namely, angle control is done separately from dc-bus control. This has shown better overall behavior, in particular regarding disturbance rejection.

Even though both controllers run on the same CPU, a decentralized control scheme is considered. When both relays are closed, the two ac-filter capacitors are lumped in one which, together with resistive load G_f, forms the weak grid admittance $\mathbf{Y}_f$. In terms of measurement, Unit 1 (grid forming) has access to its own dc link u_{dc_1}, inductor current $\boldsymbol{i}_{s_1}$, and the common ac-capacitor voltage $\boldsymbol{v}_f$ (but these latter two are not used), as well as the current drawn from the ac bus by Unit 2 (namely $\boldsymbol{i}_{s_2}$). This is required for computing $\hat{\mu}_f$ for voltage control and $\hat{P}_f$ in the droop scheme. Unit 2 (grid following) has access to u_{dc_2}, $\boldsymbol{i}_{s_2}$, and the ac-bus voltage it connects to, namely $\boldsymbol{v}_f$, which is required for computing μ_2^* and θ_2^* in the PQ-tracking scheme. The droop control (40) designed for Unit 1 was eventually not used because the angle difference is already regulated by the second converter. We have not observed any change in behavior for $\kappa_1 > 0$, while giving the same power set point $P_f^* = -P_g^*$ to Unit 1. Throughout the experiment, we fix $\kappa_1 = 0$ and $\kappa_2 = 200$. In order to track well the PQ set point, a proportional-resonant control loop was added to Unit 2 in the form of the transfer function $H_{pr}(s)$, as per Section III-E.

B. Connecting Unit 2 to Unit 1 + Load

To observe how the two systems synchronize, consider the waveforms in Fig. 15. Initially, before trigger (a) occurs, Unit 1 is disconnected from the load and Unit 2 measures zero voltage on its capacitor since both relays are open. The two units are completely independent, and they each produce a voltage on the local LC filter (seen in the initial no-load currents). The synchronizing torque is inactive on both sides and the angle difference is unregulated. At moment (a), the load G_f is connected via Relay 1 to Unit 1, which takes over the regulation of the voltage $\boldsymbol{v}_f$. At the same time, Unit 2 senses this voltage to the left of Relay 2 and so, its synchronizing torque starts driving the angle until the two systems become in phase. At moment (b), Relay 2 is closed and Unit 2 safely connects to the ac bus controlled by Unit 1 and starts tracking its given PQ set point by adjusting its magnitude and angle.

C. Tracking a Step in P_g^* (Low Line)

Fig. 16 shows the transient in active power delivered by Unit 2. We observed good PQ set point tracking performance when the internal-model compensation was added to $\boldsymbol{m}_{\alpha\beta_2}$.

Fig. 17 shows the same transient in active power as in Fig. 16. Notice the step in dc-side current i_{x_2} indicating the fast jump in power. Further observe the performance of the voltage control showing about 3% droop from full load to no load. This is mainly due to the parameter uncertainty affecting the feedforward computation of $\hat{\mu}_f$.

Fig. 18 shows the same transient in active power as in Fig. 16, but with different probed signals. Notice the well regulated dc buses, Unit 1 showing less noise and a faster transient since it is connected directly to a lab power supply.

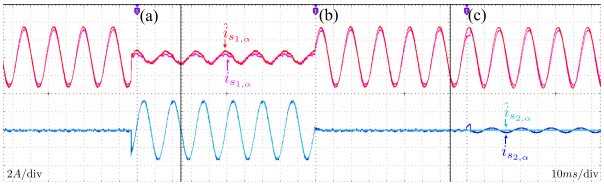

Fig. 19. Both relays are initially closed while set point P_g^* goes from 0 to 660 W (a) and back to 0 (b). Then Unit 2 is disconnected via Relay 2 at trigger (c); $Q_g^* = 0$. Showing $i_{s_{1,\alpha}}$, $\hat{i}_{s_{1,\alpha}}$, $i_{s_{2,\alpha}}$, and $\hat{i}_{s_{2,\alpha}}$.

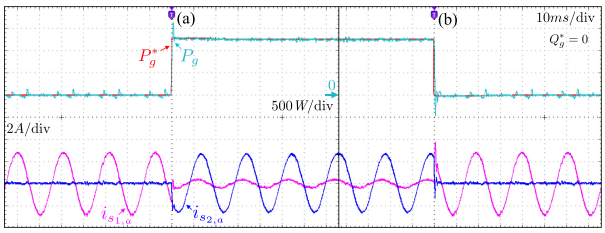

Fig. 20. Both relays are closed, while the set point P_g^* for Unit 2 goes from 0 to 1250 W at trigger (a) and then back to 0 at (b); $Q_g^* = 0$. Showing P_g^*, P_g, inductor current, phase-a, of Unit 1 and of Unit 2.

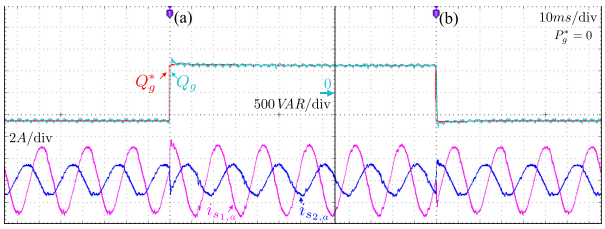

Fig. 21. Both relays are closed while the set point Q_g^* for Unit 2 goes from -625 to 625 VAR at trigger (a) and then back to -625 VAR at (b); $P_g^* = 0$. Showing Q_g^*, Q_g, inductor current, phase-a, of Unit 1 and 2.

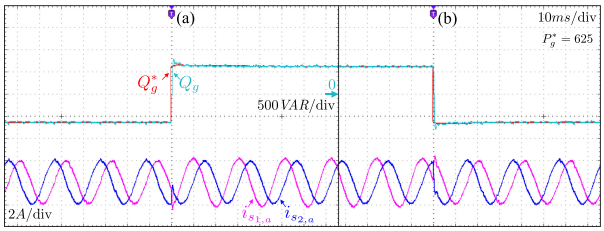

Fig. 22. Both relays are closed while the set point Q_g^* for Unit 2 goes from -625 to 625 VAR at trigger (a) and then back to -625 VAR at (b); $P_g^* = 625$. Showing Q_g^*, Q_g, inductor current, phase-a, of Unit 1 and 2.

Fig. 19 shows that the path-following objective (iii) is affected by uncertainty, particularly in Unit 1, which does not use active internal-model compensation.

D. Tracking a Step in P_g^* and in Q_g^* (High Line)

At a later stage, the hardware setup was modified to support the IEEE 50-Hz, 400-V line-to-line rms grid standard. The same controllers were deployed with as slight change in parameters to accommodate the hardware changes, a 1350-W load and the 750-Vdc bus. The PQ-tracking results, at the high-line power and voltage ratings, shown in Figs. 20–22 are similar to the ones in Section V-C.

VI. Conclusion

This article is based on the idea of modeling the dynamics of the dc bus such that the whole converter is seen as a modulated energy transfer device, i.e., a gyrator. This crucial aspect has revealed the following:

1) the inherent synchronization torque is the gradient of a function anticipating the inductor energy;
2) the large-signal transient behavior is similar to that of a damped pendulum under gravity;
3) accurate knowledge of the converter impedances facilitate the use of feedforward action;
4) the dc bus based PLL allows seamless transition between grid-following and grid-forming mode, with potential applications to islanded and black-start operations;
5) inertia and damping can be augmented by the dc-source current via PD control;
6) by injecting just the right amount of instantaneous power from the dc side, standard droop control emerges;
7) the power flow assignment adapts to the limitations of the dc-side current.

We have seen that, by adding the dc-bus integrator, we were able to exactly match the SM dynamics and produce unhampered power flow from ac to dc, merging the benefits of the electrical machine and inverter. By identifying a canonical control structure, we were able to recover the fundamental behavior of swing equations and droop control, and study the converter in a microgrid setting.

Appendix A
Synchronous Machine Model

Consider a nonsalient rotor, single-pole pair, dc-excited SM without damper windings [35], written in $\alpha\beta$ frame as

$$\frac{\mathrm{d}\theta}{\mathrm{d}t} = \omega \tag{41a}$$

$$M\frac{\mathrm{d}\omega}{\mathrm{d}t} = -D\omega - \tau_e + \tau_m \tag{41b}$$

$$\frac{\mathrm{d}\lambda_r}{\mathrm{d}t} = -R_r i_r + u_r \tag{41c}$$

$$\frac{\mathrm{d}\boldsymbol{\lambda}_s}{\mathrm{d}t} = -R_s \boldsymbol{i}_s + \boldsymbol{v}_g\,. \tag{41d}$$

Here M and D are the rotor moment of inertia and damping coefficient, θ is the rotor angle, and ω its angular velocity. We assume that the rotor is driven by the mechanical torque τ_m and has its terminals connected to a grid voltage $\boldsymbol{v}_g$, as does the inverter. We further denote τ_e as the air-gap torque, λ_r as the rotor flux linkage (scalar), i_r its current and u_r the voltage applied to the rotor terminals. Moreover, $\boldsymbol{\lambda}_s$ denotes the stator flux linkage (vector) and $\boldsymbol{i}_s$ its current. The losses in the rotor and stator are represented, respectively, by R_r and R_s.

We consider the electromagnetic energy stored in the SM

$$W_e = \frac{1}{2}\begin{bmatrix}\lambda_{s_\alpha}\\ \lambda_{s_\beta}\\ \lambda_r\end{bmatrix}^\top \begin{bmatrix} L_s & 0 & L_m\cos\theta \\ 0 & L_s & L_m\sin\theta \\ L_m\cos\theta & L_m\sin\theta & L_r\end{bmatrix}^{-1} \begin{bmatrix}\lambda_{s_\alpha}\\ \lambda_{s_\beta}\\ \lambda_r\end{bmatrix} \tag{42}$$

TABLE I
OVERVIEW OF THE CONTROLLERS FOR SOME POSSIBLE GRID-CONNECTED SCENARIOS

Function	(I) Stiff grid: VSC-L connected to $\boldsymbol{v}_g$ *set-point:* [a] (P_g^*, Q_g^*) *or* [b] (P_g^*, i_s^*)	(II) Weak grid: VSC-LC connected to $\boldsymbol{i}_g$ *set-point:* [a] (P_f^*, Q_f^*) *or* [b] (P_f^*, v_f^*)
[a] PQ tracking $\boldsymbol{i}_s \to \hat{\boldsymbol{i}}_s \to \boldsymbol{i}_s^\star$ (I) $\boldsymbol{v}_f \to \hat{\boldsymbol{v}}_f \to \boldsymbol{v}_f^\star$ (II) (grid-following)	$\boldsymbol{i}_s^\star = \frac{1}{\|\boldsymbol{v}_g\|^2}\begin{bmatrix} P_g^* & Q_g^* \\ -Q_g^* & P_g^* \end{bmatrix}\boldsymbol{v}_g$ $\mu^* = \frac{1}{u_{dc}^*}\|\boldsymbol{v}_g - \mathbf{Z}_s\boldsymbol{i}_s^\star\|$ $\begin{bmatrix} -\sin\theta^* \\ \cos\theta^* \end{bmatrix} = \frac{1}{\mu^* u_{dc}^*}\left(\boldsymbol{v}_g - \mathbf{Z}_s\boldsymbol{i}_s^\star\right)$ $\mathcal{S} = \frac{1}{2}\hat{\boldsymbol{i}}_s^\top L_s\hat{\boldsymbol{i}}_s$ $\tau_{\text{sync}} = -\nabla\mathcal{S}(\theta - \theta^*)$	$\boldsymbol{v}_f^\star = \frac{1}{\|\boldsymbol{i}_g\|^2}\begin{bmatrix} P_f^* & Q_f^* \\ -Q_f^* & P_f^* \end{bmatrix}\boldsymbol{i}_g$ $\mu^* = \frac{1}{u_{dc}^*}\|(\mathbf{Z}_s\mathbf{Y}_f + \mathbf{I})\boldsymbol{v}_f^\star + \mathbf{Z}_s\boldsymbol{i}_g\|$ $\begin{bmatrix} -\sin\theta^* \\ \cos\theta^* \end{bmatrix} = \frac{1}{\mu^* u_{dc}^*}\left((\mathbf{Z}_s\mathbf{Y}_f + \mathbf{I})\boldsymbol{v}_f^\star + \mathbf{Z}_s\boldsymbol{i}_g\right)$ $\mathcal{S} = \frac{1}{2}\hat{\boldsymbol{i}}_s^\top L_s\hat{\boldsymbol{i}}_s - \frac{1}{2}\hat{\boldsymbol{v}}_f^\top C_f\hat{\boldsymbol{v}}_f$ $\tau_{\text{sync}} = -\nabla\mathcal{S}(\theta - \theta^*)$
[b] Droop-based (grid-supporting)	$\mu = \frac{e_0}{u_{dc}^*}$ *or* $\mu = \hat{\mu}_s(\theta_{\mathsf{dq}}^*)$ $\mathcal{W}(\theta_{\mathsf{dq}}) = \frac{1}{\omega_0}(\hat{Q}_g(\theta_{\mathsf{dq}}) - \hat{Q}_g(\theta_{\mathsf{dq}}^*) - \nabla\hat{Q}_g(\theta_{\mathsf{dq}}^*)(\theta_{\mathsf{dq}} - \theta_{\mathsf{dq}}^*))$ $\tau_{\text{sync}} = -\nabla\mathcal{W}(\theta_{\mathsf{dq}}) = -\frac{1}{\omega_0}(\hat{P}_g(\theta_{\mathsf{dq}}) - P_g^*)$	$\mu = \frac{\|\mathbf{Z}_s\mathbf{Y}_f + \mathbf{I}\|v_f^*}{u_{dc}^*}$ *or* $\mu = \hat{\mu}_f(\theta_{\mathsf{dq}}^*)$ $\mathcal{W}(\theta_{\mathsf{dq}}) = \frac{1}{\omega_0}(\hat{Q}_f(\theta_{\mathsf{dq}}) - \hat{Q}_f(\theta_{\mathsf{dq}}^*) - \nabla\hat{Q}_f(\theta_{\mathsf{dq}}^*)(\theta_{\mathsf{dq}} - \theta_{\mathsf{dq}}^*))$ $\tau_{\text{sync}} = -\nabla\mathcal{W}(\theta_{\mathsf{dq}}) = -\frac{1}{\omega_0}(\hat{P}_f(\theta_{\mathsf{dq}}) - P_f^*)$

where L_s and L_r are the stator and rotor self-inductances, respectively, and L_m is the mutual inductance of the machine. Accordingly, the electrical quantities are related as

$$\tau_e = \frac{\partial W_e}{\partial\theta} = -L_m i_r \begin{bmatrix} -\sin\theta \\ \cos\theta \end{bmatrix}^\top \boldsymbol{i}_s \tag{43a}$$

$$i_r = \frac{\partial W_e}{\partial\lambda_r} \Leftrightarrow \lambda_r = L_r i_r + L_m \begin{bmatrix} \cos\theta \\ \sin\theta \end{bmatrix}^\top \boldsymbol{i}_s \tag{43b}$$

$$\boldsymbol{i}_s^\top = \frac{\partial W_e}{\partial\boldsymbol{\lambda}_s} \Leftrightarrow \boldsymbol{\lambda}_s = L_s\boldsymbol{i}_s + L_m \begin{bmatrix} \cos\theta \\ \sin\theta \end{bmatrix} i_r. \tag{43c}$$

Using Faraday's law, we define the rotor and stator EMF as $e_r = \frac{\mathsf{d}}{\mathsf{d}t}(\lambda_r - L_r i_r)$ and, respectively, $\boldsymbol{e}_s = \frac{\mathsf{d}}{\mathsf{d}t}(\boldsymbol{\lambda}_s - L_s\boldsymbol{i}_s)$, which we expand in the following:

$$\boldsymbol{e}_s = L_m i_r \begin{bmatrix} -\sin\theta \\ \cos\theta \end{bmatrix}\omega + L_m \frac{\mathsf{d}i_r}{\mathsf{d}t}\begin{bmatrix} \cos\theta \\ \sin\theta \end{bmatrix}. \tag{44}$$

Suppose now that the rotor current is regulated to a constant i_r^* via a control, such as $u_r = R_r i_r^* + e_r$. As a consequence, when $i_r = i_r^*$, (41c) becomes $L_r\frac{\mathsf{d}i_r}{\mathsf{d}t} = 0$, so it can be set aside. The system reduces to (7).

APPENDIX B
ENERGY-BASED STABILIZATION OF THE eSM

Consider the eSM (11), in the stiff grid scenario of Section III-A and written in coordinates θ_{dq}, $\tilde{u}_{\text{dc}}$, $\tilde{\boldsymbol{i}}_{\mathsf{dq}} = \boldsymbol{i}_{\mathsf{dq}} - \hat{\boldsymbol{i}}_{\mathsf{dq}}$ and with the input transformation $\tilde{i}_{\text{dc}} = i_{\text{dc}} - G_{\text{dc}}u_{\text{dc}}^*$

$$\frac{\mathsf{d}\theta_{\mathsf{dq}}}{\mathsf{d}t} = \eta\tilde{u}_{\text{dc}} \tag{45a}$$

$$C_{\text{dc}}\frac{\mathsf{d}\tilde{u}_{\text{dc}}}{\mathsf{d}t} = -G_{\text{dc}}\tilde{u}_{\text{dc}} + \tilde{i}_{\text{dc}} - \hat{i}_x + \mu\begin{bmatrix} -\sin\theta_{\mathsf{dq}} \\ \cos\theta_{\mathsf{dq}} \end{bmatrix}^\top \tilde{\boldsymbol{i}}_{\mathsf{dq}} \tag{45b}$$

$$L_s\frac{\mathsf{d}\tilde{\boldsymbol{i}}_{\mathsf{dq}}}{\mathsf{d}t} = -\mathbf{Z}_s\tilde{\boldsymbol{i}}_{\mathsf{dq}} - R_s\mathbf{Z}_s^{-1}\mu\begin{bmatrix} -\sin\theta_{\mathsf{dq}} \\ \cos\theta_{\mathsf{dq}} \end{bmatrix}\tilde{u}_{\text{dc}}. \tag{45c}$$

Consider again the energy function (21), accounting for the deviation from the origin of the transient system (45), as

$$\tilde{\mathcal{H}}(\theta_{\mathsf{dq}}, \tilde{u}_{\text{dc}}, \tilde{\boldsymbol{i}}_{\mathsf{dq}}) = \frac{1}{2}C_{\text{dc}}\tilde{u}_{\text{dc}}^2 + \frac{1}{2}\tilde{\boldsymbol{i}}_{\mathsf{dq}}^\top L_s\tilde{\boldsymbol{i}}_{\mathsf{dq}} + \mathcal{S}(\theta_{\mathsf{dq}}).$$

In the spirit of passivity-based control, input (17) is chosen such that it renders $\tilde{\mathcal{H}}$ decreasing along the error trajectories

$$\frac{\mathsf{d}\tilde{\mathcal{H}}}{\mathsf{d}t} = -(G_{\text{dc}} + K_p)\tilde{u}_{\text{dc}}^2 - \tilde{\boldsymbol{i}}_{\mathsf{dq}}^\top R_s\tilde{\boldsymbol{i}}_{\mathsf{dq}} - \tilde{\boldsymbol{i}}_{\mathsf{dq}}^\top T(\theta_{\mathsf{dq}})\tilde{u}_{\text{dc}}$$

where $T(\theta_{\mathsf{dq}}) = \mu\omega_0 L_s\mathbf{Z}_s^{-1}\left[\begin{smallmatrix} \cos\theta_{\mathsf{dq}} \\ \sin\theta_{\mathsf{dq}} \end{smallmatrix}\right]$. To guarantee that $\frac{\mathsf{d}\tilde{\mathcal{H}}}{\mathsf{d}t}$ is negative definite in $(\tilde{u}_{\text{dc}}, \tilde{\boldsymbol{i}}_{\mathsf{dq}})$, it is sufficient to assign K_p such that $\frac{G_{\text{dc}} + K_p}{\eta^2} > \frac{L_s^2}{4R_s}\frac{\mu^2 u_{\text{dc}}^{*2}}{\|\mathbf{Z}_s\|^2}$. This, together with boundedness of the angle, sets up the conditions to apply the LaSalle invariance principle and conclude that all trajectories $(\theta_{\mathsf{dq}}, \tilde{u}_{\text{dc}}, \tilde{\boldsymbol{i}}_{\mathsf{dq}})$ of the transient system (45) globally converge to the set of points where $\tilde{u}_{\text{dc}} = 0$, $\nabla\mathcal{S}(\theta_{\mathsf{dq}}) = 0$, and $\tilde{\boldsymbol{i}}_{\mathsf{dq}} = 0$, thus achieving the intended objectives (i), (ii), and (iii), respectively.

APPENDIX C
DERIVATION OF THE REACTIVE POWER GRADIENT

We define $\boldsymbol{i}_{g,\mathsf{dq}} = \mathbf{R}_{\theta_g}^\top\boldsymbol{i}_g$ and consider (31b) in (32) in grid-attached dq frame with modulation length $\mu = \mu_f^*$

$$\begin{aligned}
&\hat{P}_f(\theta_{\mathsf{dq}}) - \hat{P}_f(\theta_{\mathsf{dq}}^*) \\
&= \boldsymbol{i}_{g,\mathsf{dq}}^\top(\mathbf{Z}_s\mathbf{Y}_f + \mathbf{I})^{-1}\left(\mu u_{\text{dc}}^*\begin{bmatrix} -\sin\theta_{\mathsf{dq}} \\ \cos\theta_{\mathsf{dq}} \end{bmatrix} - \mathbf{Z}_s\boldsymbol{i}_{g,\mathsf{dq}}\right) \\
&\quad - \boldsymbol{i}_{g,\mathsf{dq}}^\top(\mathbf{Z}_s\mathbf{Y}_f + \mathbf{I})^{-1}\left(\mu u_{\text{dc}}^*\begin{bmatrix} -\sin\theta_{\mathsf{dq}}^* \\ \cos\theta_{\mathsf{dq}}^* \end{bmatrix} - \mathbf{Z}_s\boldsymbol{i}_{g,\mathsf{dq}}\right) \\
&= \boldsymbol{i}_{g,\mathsf{dq}}^\top\begin{bmatrix} 0 & 1 \\ -1 & 0 \end{bmatrix}(\mathbf{Z}_s\mathbf{Y}_f + \mathbf{I})^{-1} \\
&\quad \times\left(-\mu u_{\text{dc}}^*\begin{bmatrix} \cos\theta_{\mathsf{dq}} \\ \sin\theta_{\mathsf{dq}} \end{bmatrix} + \mu u_{\text{dc}}^*\begin{bmatrix} \cos\theta_{\mathsf{dq}}^* \\ \sin\theta_{\mathsf{dq}}^* \end{bmatrix}\right) \\
&= \nabla\hat{Q}_f(\theta_{\mathsf{dq}}) - \nabla\hat{Q}_f(\theta_{\mathsf{dq}}^*).
\end{aligned}$$

In the stiff-grid scenario of Section III-D, the same relationship can be derived between $\hat{P}_g$ and $\nabla\hat{Q}_g$ using (13) and (23).

REFERENCES

[1] J. I. Leon, S. Kouro, L. G. Franquelo, J. Rodriguez, and B. Wu, "The essential role and the continuous evolution of modulation techniques for voltage-source inverters in the past, present, and future power electronics," *IEEE Trans. Ind. Electron.*, vol. 63, no. 5, pp. 2688–2701, May 2016.

[2] J. Rocabert, A. Luna, F. Blaabjerg, and P. Rodriguez, "Control of power converters in ac microgrids," *IEEE Trans. Power Electron.*, vol. 27, no. 11, pp. 4734–4749, Nov. 2012.
[3] F. Blaabjerg, R. Teodorescu, M. Liserre, and A. Timbus, "Overview of control and grid synchronization for distributed power generation systems," *IEEE Trans. Ind. Electron.*, vol. 53, no. 5, pp. 1398–1409, Oct. 2006.
[4] M. G. Taul, X. Wang, P. Davari, and F. Blaabjerg, "An overview of assessment methods for synchronization stability of grid-connected converters under severe symmetrical grid faults," *IEEE Trans. Power Electron.*, vol. 34, no. 10, pp. 9655–9670, Oct. 2019.
[5] M. Malinowski, M. Kazmierkowski, S. Hansen, F. Blaabjerg, and G. Marques, "Virtual-flux-based direct power control of three-phase PWM rectifiers," *IEEE Trans. Ind. Appl.*, vol. 37, no. 4, pp. 1019–1027, Jul./Aug. 2001.
[6] Y. Gui, X. Wang, and F. Blaabjerg, "Vector current control derived from direct power control for grid-connected inverters," *IEEE Trans. Power Electron.*, vol. 34, no. 9, pp. 9224–9235, Sep. 2019.
[7] F. Milano, F. Dörfler, G. Hug, D. J. Hill, and G. Verbič, "Foundations and challenges of low-inertia systems," in *Proc. Power Syst. Comput. Conf.*, 2018, pp. 1–25.
[8] M. Farrokhabadi *et al.*, "Microgrid stability definitions, analysis, and examples," *IEEE Trans. Power Syst*. [Online]. Available: https://ieeexplore.ieee.org/stamp/stamp.jsp?arnumber=8750828
[9] L. Huang, H. Xin, and Z. Wang, "Damping low-frequency oscillations through VSC-HVDC stations operated as virtual synchronous machines," *IEEE Trans. Power Electron.*, vol. 34, no. 6, pp. 5803–5818, 2018.
[10] S. D'Arco and J. A. Suul, "Virtual synchronous machines-classification of implementations and analysis of equivalence to droop controllers for microgrids," in *Proc. IEEE Grenoble Conf.*, 2013, pp. 1–7.
[11] H. Bevrani, T. Ise, and Y. Miura, "Virtual synchronous generators: A survey and new perspectives," *Int. J. Elect. Power Energy Syst.*, vol. 54, pp. 244–254, 2014.
[12] L. Xiong *et al.*, "Static synchronous generator model: A new perspective to investigate dynamic characteristics and stability issues of grid-tied PWM inverter," *IEEE Trans. Power Electron.*, vol. 31, no. 9, pp. 6264–6280, Sep. 2016.
[13] B. Wen, D. Boroyevich, R. Burgos, P. Mattavelli, and Z. Shen, "Analysis of DQ small-signal impedance of grid-tied inverters," *IEEE Trans. Power Electron.*, vol. 31, no. 1, pp. 675–687, Jan. 2016.
[14] X. Wang, L. Harnefors, and F. Blaabjerg, "Unified impedance model of grid-connected voltage-source converters," *IEEE Trans. Power Electron.*, vol. 33, no. 2, pp. 1775–1787, Feb. 2018.
[15] A. Tayyebi, D. Groß, A. Anta, F. Kupzog, and F. Dörfler, "Interactions of grid-forming power converters and synchronous machines–A comparative study," 2019, *arXiv:1902.10750*.
[16] C. Zhang, M. Molinas, X. Cai, and A. Rygg, "Understanding the nonlinear behavior and frequency stability of a grid-synchronized VSC under grid voltage dips," 2018, *arXiv:1806.11529*.
[17] R. Ortega, A. Van Der Schaft, F. Castanos, and A. Astolfi, "Control by interconnection and standard passivity-based control of port-Hamiltonian systems," *IEEE Trans. Autom. Control*, vol. 53, no. 11, pp. 2527–2542, Dec. 2008.
[18] A. Aguiar, J. Hespanha, and P. Kokotovic, "Path-following for nonminimum phase systems removes performance limitations," *IEEE Trans. Autom. Control*, vol. 50, no. 2, pp. 234–239, Feb. 2005.
[19] C. Byrnes and A. Isidori, "Output regulation for nonlinear systems: An overview," *Int. J. Robust Nonlinear Control: IFAC-Affiliated J.*, vol. 10, no. 5, pp. 323–337, 2000.
[20] I. Cvetkovic, D. Boroyevich, R. Burgos, C. Li, M. Jaksic, and P. Mattavelli, "Modeling of a virtual synchronous machine-based grid-interface converter for renewable energy systems integration," in *Proc. IEEE 15th Workshop Control Model. Power Electron.*, 2014, pp. 1–7.
[21] I. Cvetkovic, D. Boroyevich, R. Burgos, C. Li, and P. Mattavelli, "Modeling and control of grid-connected voltage-source converters emulating isotropic and anisotropic synchronous machines," in *Proc. IEEE 16th Workshop Control Model. Power Electron.*, 2015, pp. 1–5.
[22] T. Jouini, C. Arghir, and F. Dörfler, "Grid-friendly matching of synchronous machines by tapping into the dc storage," *IFAC-PapersOnLine*, vol. 49, no. 22, pp. 192–197, 2016.
[23] C. Arghir, T. Jouini, and F. Dörfler, "Grid-forming control for power converters based on matching of synchronous machines," *Automatica*, vol. 95, pp. 273–282, 2018.
[24] C. Li, I. Cvetkovic, R. Burgos, and D. Boroyevich, "Assessment of virtual synchronous machine based control in grid-tied power converters," in *Proc. Int. Power Electron. Conf.*, May 2018, pp. 790–794.
[25] L. Huang *et al.*, "A virtual synchronous control for voltage-source converters utilizing dynamics of dc-link capacitor to realize self-synchronization," *IEEE J. Emerg. Sel. Topics Power Electron.*, vol. 5, no. 4, pp. 1565–1577, Dec. 2017.
[26] N. Barrera Gallegos, M. Victoria Gasca, and M. Molinas, "Synchronization properties of voltage source converters when seen as coupled oscillators based on the Kuramoto model," in *Proc. 9th Vienna Int. Conf. Math. Model.*, 2018.
[27] T. Noguchi, H. Tomiki, S. Kondo, and I. Takahashi, "Direct power control of PWM converter without power source voltage sensors," in *Proc. Conf. Rec. IEEE Ind. Appl. Conf. 31st IAS Annu. Meet.*, 1996, vol. 2, 1996, pp. 941–946.
[28] G. Escobar, A. M. Stankovic, J. M. Carrasco, E. Galván, and R. Ortega, "Analysis and design of direct power control (DPC) for a three phase synchronous rectifier via output regulation subspaces," *IEEE Trans. Power Electron.*, vol. 18, no. 3, pp. 823–830, May 2003.
[29] A. Rantzer, "Almost global stability of phase-locked loops," in *Proc. 40th IEEE Conf. Decis. Control*, vol. 1, 2001, pp. 899–900.
[30] B. A. Francis and W. M. Wonham, "The internal model principle of control theory," *Automatica*, vol. 12, no. 5, pp. 457–465, 1976.
[31] F. Dorfler and F. Bullo, "Synchronization and transient stability in power networks and nonuniform Kuramoto oscillators," *SIAM J. Control Optim.*, vol. 50, no. 3, pp. 1616–1642, 2012.
[32] C. Arghir and F. Dörfler, "Energy-based stabilization of network flows in multi-machine power systems," in *Proc. 23rd Int. Symp. Math. Theory Netw. Syst.*, 2018.
[33] C. De Persis and N. Monshizadeh, "Bregman storage functions for microgrid control," *IEEE Trans. Autom. Control*, vol. 63, no. 1, pp. 53–68, Jan. 2018.
[34] Imperix, *PEB8032*. [Online]. Available: https://imperix.ch/products/power/peb
[35] J. Machowski, J. Bialek, and J. Bumby, *Power System Dynamics: Stability and Control*. Hoboken, NJ, USA: Wiley, 2011.

Catalin Arghir received the Diploma degree from the Polytechnic University of Bucharest, Bucharest, Romania, in 2009, and the M.Eng. degree in electrical and computer engineering from the University of Toronto, Toronto, ON, Canada, in 2014. He is currently working toward the Ph.D. degree under the guidance of Prof. Florian Drfler with ETH Zurich, Zurich, Switzerland.

From 2012 to 2014, he was with Murata Power Solutions, Markham, ON, Canada, where he developed control firmware for power converters. He is currently a Research Assistant with the Automatic Control Laboratory, ETH Zurich, where he is working on nonlinear and geometric control techniques for power electronics and power systems applications.

Florian Dörfler received the Diploma degree in engineering cybernetics from the University of Stuttgart, Stuttgart, Germany, in 2008, and the Ph.D. degree in mechanical engineering from the University of California at Santa Barbara, Santa Barbara, CA, USA, in 2013.

From 2013 to 2014, he was an Assistant Professor with the University of California, Los Angeles, CA, USA. He is an Associate Professor with the Automatic Control Laboratory at ETH Zurich, Zurich, Switzerland.

Dr. Dorfler was the recipient of 2009 Regents Special International Fellowship, the 2010 ACC Student Best Paper Award, the 2011 O. Hugo Schuck Best Paper Award, the 2011 Peter J. Frenkel Foundation Fellowship, the 2012–2014 Automatica Best Paper Award, the 2015 UCSB ME Best Ph.D. Award, and the 2016 IEEE Circuits and Systems Guillemin-Cauer Best Paper Award.